

Differentiable MADNIS-Lite

Theo Heimel¹, Olivier Mattelaer², Tilman Plehn^{1,3}, and Ramon Winterhalder²

¹ Institut für Theoretische Physik, Universität Heidelberg, Germany

² CP3, Université catholique de Louvain, Louvain-la-Neuve, Belgium

³ Interdisciplinary Center for Scientific Computing (IWR), Universität Heidelberg, Germany

August 6, 2024

Abstract

Differentiable programming opens exciting new avenues in particle physics, also affecting future event generators. These new techniques boost the performance of current and planned MadGraph implementations. Combining phase-space mappings with a set of very small learnable flow elements, MADNIS-Lite, can improve the sampling efficiency while being physically interpretable. This defines a third sampling strategy, complementing VEGAS and the full MADNIS.

Contents

1	Introduction	2
2	MADNIS basics	2
3	Differentiable integrand	4
3.1	Forward and inverse training	5
3.2	Loss landscape	7
4	Differentiable phase space — MADNIS-Lite	9
4.1	Parameterized mappings	9
4.2	Learnable bilinear spline flows	12
5	Outlook	16
A	Hyperparameters	18
B	Analytic loss function gradients	18
C	Explicit channel mapping	21
	References	23

1 Introduction

The incredibly successful precision-LHC program is based on comparing vast numbers of scattering events with first-principle predictions provided by multi-purpose event generators, like PYTHIA8 [1], MG5AMC [2], and SHERPA [3]. For a given Lagrangian, they use perturbative quantum field theory to provide the backbone of a complex simulation and inference chain. In view of the upcoming LHC runs, we will have to rely on modern machine learning (ML) [4, 5] to significantly improve the speed and the precision of these simulations, for instance through MADNIS [6, 7]. Following the modular structure of event generators, such modern neural networks will transform scattering amplitude evaluations [8–14], phase-space sampling [6, 15–24], event generation [25–31], parton shower generation [32–39], as well as the critical and currently far too slow detector simulations [40–67].

The workhorses for this transformation are generative networks, currently trained on and amplifying simulated training data [68, 69]. Given the LHC requirements, they have to be controlled and precise in encoding kinematic patterns over an, essentially, interpretable phase space [30, 70–73]. In addition to event generation, these generative networks can be used for event subtraction [74], event unweighting [75, 76], or super-resolution enhancement [77, 78]. Their conditional versions enable new analysis methods, like probabilistic unfolding [79–88], inference [89–92], or anomaly detection [93–98].

An even more advanced strategy to improve LHC simulations is differentiable programming. Here, the entire simulation chain is envisioned to benefit from the availability of derivatives with respect to, for instance, model and tuning parameters in modern computer languages. A proof of principle has been delivered for differentiable matrix elements [99], but the same methods are used for differentiable detector design [100], derivatives of branching processes [101], shower-simulations with path-wise derivatives [102], all the way to a differentiable parton-shower event generator for e^+e^- collisions [103]. The crucial question is where differentiable programming can be used to improve existing ML-enhanced classic event generators.

We will test how a differentiable version of the MADNIS event sampler [6, 7] compares to established improvements which will be part of an upcoming MADGRAPH release for the HL-LHC. We expect our findings to similarly apply to neural importance sampling (NIS) developments in SHERPA [18, 19]. In Sec. 2 we briefly review the MADNIS reference structures, into which we first implement a differentiable integrand, including phase space, matrix element, and parton densities, in Sec. 3. In a second step, we construct a differentiable phase space generator to improve the phase space mapping through a set of small learnable elements, MADNIS-Lite, in Sec. 4. Here we find that differentiable programming can be useful for ML-event generators, but the performance gain has to be benchmarked and evaluated carefully. For MADNIS-Lite, a differentiable phase space generator appears very promising.

2 MADNIS basics

We briefly review multi-channel Monte Carlo and the MADNIS basics [6, 7], necessary to understand the subsequent sections. We consider the integral of a function $f \sim |\mathcal{M}|^2$ over phase space

$$I[f] = \int dx f(x) \quad x \in \mathbb{R}^D. \quad (1)$$

It can be decomposed by introducing local channel weights $\alpha_i(x)$ [104, 105]

$$f(x) = \sum_{i=1}^{n_c} \alpha_i(x) f(x) \quad \text{with} \quad \sum_{i=1}^{n_c} \alpha_i(x) = 1 \quad \text{and} \quad \alpha_i(x) \geq 0, \quad (2)$$

using the MG5AMC decomposition. Similar decompositions [106, 107] are used in SHERPA [3] and WHIZARD [108]. The phase-space integral now reads

$$I[f] = \sum_{i=1}^{n_c} \int dx \alpha_i(x) f(x). \quad (3)$$

Next, we introduce a set of channel-dependent phase-space mappings

$$x \in \mathbb{R}^D \quad \begin{array}{c} \xleftarrow{G_i(x) \rightarrow} \\ \xrightarrow{\leftarrow \bar{G}_i(z)} \end{array} \quad z \in [0, 1]^D, \quad (4)$$

which parametrize properly normalized densities

$$g_i(x) = \left| \frac{\partial G_i(x)}{\partial x} \right| \quad \text{with} \quad \int dx g_i(x) = 1. \quad (5)$$

The phase-space integral now covers the D -dimensional unit hypercube and is sampled as

$$\begin{aligned} I[f] &= \sum_{i=1}^{n_c} \int \frac{dz}{g_i(x)} \alpha_i(x) f(x) \Big|_{x=\bar{G}_i(z)} \\ &= \sum_{i=1}^{n_c} \int dx g_i(x) \frac{\alpha_i(x) f(x)}{g_i(x)} \equiv \sum_{i=1}^{n_c} \left\langle \frac{\alpha_i(x) f(x)}{g_i(x)} \right\rangle_{x \sim g_i(x)}. \end{aligned} \quad (6)$$

This is the basis of multi-channel importance sampling [107]. Starting from this equation, MADNIS encodes the multi-channel weight $\alpha_i(x)$ and the channel mappings $G_i(x)$ in neural networks.

Neural channel weights

First, MADNIS employs a channel-weight network to encode the local multi-channel weights

$$\alpha_i(x) \equiv \alpha_{i\xi}(x), \quad (7)$$

where ξ denotes the network parameters. As the channel weights vary strongly over phase space, it helps the performance to learn them as a correction to a physically motivated prior assumption like [104, 105]

$$\begin{aligned} \alpha_i^{\text{MG}}(x) &= \frac{|\mathcal{M}_i(x)|^2}{\sum_j |\mathcal{M}_j(x)|^2} \\ \alpha_i^{\text{MG}}(x) &= \frac{P_i(x)}{\sum_j P_j(x)} \quad \text{with} \quad P_i(x) = \prod_{k \in \text{prop}} \frac{1}{|p_k(x)^2 - m_k^2 - im_k \Gamma_k|^2}. \end{aligned} \quad (8)$$

Relative to either of them, we then only learn a correction factor [7].

Neural importance sampling

Second, MADNIS combines analytic channel mappings with a normalizing flow [109, 110],

$$x \in \mathbb{R}^D \xleftrightarrow{\text{analytic}} y \in [0, 1]^D \xleftrightarrow{\text{flow}} z \in [0, 1]^D, \quad (9)$$

to complement VEGAS [111–113]. The flow allows MADNIS to improve the physics-inspired phase-space mappings by training a network to map

$$z = G_{i\theta}(x) \quad \text{or} \quad x = \bar{G}_{i\theta}(z). \quad (10)$$

As for the channel weights, we use physics knowledge to simplify the ML task and a VEGAS pre-training [7]. This makes use of the key strength of VEGAS, which is extremely efficient for factorizing integrands and converges much faster than neural importance sampling.

Multi-channel variance loss

With the channel weights and importance sampling encoded in neural networks,

$$\alpha_i(x) \equiv \alpha_{i\xi}(x) \quad \text{and} \quad g_i(x) \equiv g_{i\theta}(x), \quad (11)$$

the integral in Eq.(6) becomes

$$I[f] = \sum_{i=1}^{n_c} \left\langle \frac{\alpha_{i\xi}(x)f(x)}{g_{i\theta}(x)} \right\rangle_{x \sim g_{i\theta}(x)}. \quad (12)$$

Crucially, we then minimize the variance as the loss [6, 7]

$$\begin{aligned} \mathcal{L}_{\text{variance}} &= \sum_{i=1}^{n_c} \frac{N}{N_i} \sigma_i^2 \\ &= \sum_{i=1}^{n_c} \frac{N}{N_i} \left(\left\langle \frac{\alpha_{i\xi}(x)^2 f(x)^2}{g_{i\theta}(x) q_i(x)} \right\rangle_{x \sim q_i(x)} - \left\langle \frac{\alpha_{i\xi}(x) f(x)}{q_i(x)} \right\rangle_{x \sim q_i(x)}^2 \right). \end{aligned} \quad (13)$$

In practice, $q_i(x) \simeq g_{i\theta}(x)$ allows us to compute the loss as precisely as possible and stabilizes the combined online [114] and buffered training [6]. Inspired by stratified sampling, we encode the optimal choice for N_i [107, 115] in the MADNIS loss [7]

$$\begin{aligned} \mathcal{L}_{\text{MADNIS}} &= \sum_{i=1}^{n_c} \left(\sum_{j=1}^{n_c} \sigma_j \right) \sigma_i = \left[\sum_{i=1}^{n_c} \sigma_i \right]^2 \\ &= \left[\sum_{i=1}^{n_c} \left(\left\langle \frac{\alpha_{i\xi}(x)^2 f(x)^2}{g_{i\theta}(x) q_i(x)} \right\rangle_{x \sim q_i(x)} - \left\langle \frac{\alpha_{i\xi}(x) f(x)}{q_i(x)} \right\rangle_{x \sim q_i(x)}^2 \right)^{1/2} \right]^2. \end{aligned} \quad (14)$$

3 Differentiable integrand

To investigate how the choice of the loss function and the direction of the training affects the performance of MADNIS, we consider a realistic LHC process, namely triple-W production,

$$u\bar{d} \rightarrow W^+W^+W^- \quad (15)$$

At leading order, this process comes with 17 Feynman diagrams and 16 integration channels in MG5AMC. It has been shown to benefit significantly from ML-based importance sampling methods [7] and that a single fine-tuned integration channel is sufficient to achieve good performance. We have implemented a simple differentiable event generator for this process in MADNIS, including

- a differentiable squared matrix element using helicity amplitudes natively written in PYTORCH that are generated from our custom MG5AMC plugin similar to MADFLOW [116] and MADJAX [99];
- a differentiable and invertible phase-space generator based on RAMBOONDIET [71, 117, 118] natively written in PYTORCH. A similar implementation has been used in MADJAX [99];
- and differentiable parton densities using the standard LHAPDF interpolation [119] natively written in PYTORCH which is similar to PDFFLOW [120] relying on TENSORFLOW.

3.1 Forward and inverse training

As a starting point we consider a generic F -divergence [121] between two normalized probability distributions $p_1(z)$ and $p_2(z)$,

$$D_F^z[p_1, p_2] = \int dz p_2(z) F\left(\frac{p_1(z)}{p_2(z)}\right). \quad (16)$$

For a MADNIS-like training, we have a target function $f(x)$ and a normalizing flow that parametrizes a trainable invertible mapping with network parameters θ

$$x \begin{array}{c} \xleftarrow{G_\theta(x) \rightarrow} \\ \xrightarrow{\leftarrow \bar{G}_\theta(z)} \end{array} z \quad (17)$$

and induces the density distribution

$$g_\theta(x) = p_0(G_\theta(x)) \left| \frac{\partial G_\theta(x)}{\partial x} \right|, \quad (18)$$

with latent space distribution $p_0(z)$. For convenience, we can also define

$$\bar{g}_\theta(z) = p_0(z) \left| \frac{\partial \bar{G}_\theta(z)}{\partial z} \right|^{-1} \quad \text{such that} \quad \bar{g}_\theta(G_\theta(x)) = g_\theta(x). \quad (19)$$

Note that $g_\theta(x)$ is a normalized probability distribution in x -space (data space), but this is not the case for $\bar{g}_\theta(z)$ in z -space (latent space). There are two ways to define a loss function to train the flow. First, we define the loss function in data space,

$$\mathcal{L}_F^{\text{fw}} = D_F^x[f, g_\theta] = \int dx g_\theta(x) F\left(\frac{f(x)}{g_\theta(x)}\right) = \left\langle \frac{g_\theta(x)}{q(x)} F\left(\frac{f(x)}{g_\theta(x)}\right) \right\rangle_{x \sim q(x)}. \quad (20)$$

In the last step, we introduce an importance sampling distribution $q(x)$ to evaluate the integral numerically. This can be the same as $g_\theta(x)$ for online training, or different for buffered training [7]. Optimizing this loss function requires evaluating the flow in the forward direction according to Eq.(18), so we refer to this training mode as forward training.

Alternatively, we can train in latent space using the remapped target distribution

$$\hat{f}(z) = f(\bar{G}_\theta(z)) \left| \frac{\partial \bar{G}_\theta(z)}{\partial z} \right|, \quad (21)$$

which is a normalized probability in latent space according to the change of variables formula. During training we minimize the divergence between $\hat{f}(z)$ and the latent space distribution

$$\begin{aligned}\mathcal{L}_F^{\text{inv}} &= D_F^z[f, p_0] = \int dz p_0(z) F\left(\frac{\hat{f}(z)}{p_0(z)}\right) \\ &= \int dz p_0(z) F\left(\frac{f(\bar{G}_\theta(z))}{p_0(z)} \left| \frac{\partial \bar{G}_\theta(z)}{\partial z} \right| \right) \\ &= \int dz p_0(z) F\left(\frac{f(\bar{G}_\theta(z))}{\bar{g}_\theta(z)}\right) = \left\langle F\left(\frac{f(\bar{G}_\theta(z))}{\bar{g}_\theta(z)}\right) \right\rangle_{z \sim p_0(z)}.\end{aligned}\quad (22)$$

We refer to this as inverse training because we evaluate the flow in the inverse direction. Note that this inverse training requires a differentiable integrand which is not needed in the forward training. It turns out that the forward and inverse training yield the same result for the loss,

$$\begin{aligned}\mathcal{L}_F^{\text{inv}} &= \int dx p_0(G_\theta(x)) \left| \frac{\partial G_\theta(x)}{\partial x} \right| F\left(\frac{f(\bar{G}_\theta(G_\theta(x)))}{\bar{g}_\theta(G_\theta(x))}\right) \\ &= \int dx g_\theta(x) F\left(\frac{f(x)}{g_\theta(x)}\right) = \mathcal{L}_F^{\text{fw}}.\end{aligned}\quad (23)$$

Loss gradients

Because the two losses are identical, the gradients of the forward and inverse loss functions have the same expectation value,

$$\nabla_\theta \mathcal{L}_F^{\text{inv}} = \left\langle \nabla_\theta F\left(\frac{f(\bar{G}_\theta(z))}{\bar{g}_\theta(z)}\right) \right\rangle_{z \sim p_0(z)} = \left\langle \nabla_\theta \frac{g_\theta(x)}{q(x)} F\left(\frac{f(x)}{g_\theta(x)}\right) \right\rangle_{x \sim q(x)} = \nabla_\theta \mathcal{L}_F^{\text{fw}}. \quad (24)$$

From these expressions we can see that the two methods are not equivalent for the variances of the gradients. For the inverse training, it is

$$\begin{aligned}\text{Var}_{z \sim p_0(z)}\left(\nabla_\theta F\left(\frac{f(\bar{G}_\theta(z))}{\bar{g}_\theta(z)}\right)\right) &= \left\langle \left(\nabla_\theta F\left(\frac{f(\bar{G}_\theta(z))}{\bar{g}_\theta(z)}\right) - \nabla_\theta \mathcal{L}_F^{\text{inv}}\right)^2 \right\rangle_{z \sim p_0(z)} \\ &= \int dz p_0(z) \left(\nabla_\theta F\left(\frac{f(\bar{G}_\theta(z))}{\bar{g}_\theta(z)}\right) - \nabla_\theta \mathcal{L}_F^{\text{inv}}\right)^2,\end{aligned}\quad (25)$$

while for the forward direction, we find

$$\begin{aligned}\text{Var}_{x \sim q(x)}\left(\nabla_\theta \frac{g_\theta(x)}{q(x)} F\left(\frac{f(x)}{g_\theta(x)}\right)\right) &= \left\langle \left(\nabla_\theta \frac{g_\theta(x)}{q(x)} F\left(\frac{f(x)}{g_\theta(x)}\right) - \nabla_\theta \mathcal{L}_F^{\text{fw}}\right)^2 \right\rangle_{x \sim q(x)} \\ &= \int dx q(x) \left(\nabla_\theta \frac{g_\theta(x)}{q(x)} F\left(\frac{f(x)}{g_\theta(x)}\right) - \nabla_\theta \mathcal{L}_F^{\text{fw}}\right)^2.\end{aligned}\quad (26)$$

In general, the two will not be equal. Depending on the problem and choice of F -divergence, one of the two training modes can have noisier gradients, leading to a slower convergence of the training on finite batch sizes. In Appendix B, we study this behavior by analytically solving a simple 1D-toy example.

3.2 Loss landscape

Finally, we look at established examples of divergences used to construct loss functions. They use a normalized target distribution $f(x)$, which can be ensured during training by using batch-wise normalization of the integrand values:

- variance, $F(t) = (t - 1)^2$

$$\begin{aligned}\mathcal{L}_{\text{var}}^{\text{fw}} &= \left\langle \frac{g_\theta(x)}{q(x)} \left(\frac{f(x)}{g_\theta(x)} - 1 \right)^2 \right\rangle_{x \sim q(x)} \\ \mathcal{L}_{\text{var}}^{\text{inv}} &= \left\langle \left(\frac{f(\bar{G}_\theta(z))}{\bar{g}_\theta(z)} - 1 \right)^2 \right\rangle_{z \sim p_0(z)}.\end{aligned}\quad (27)$$

- KL-divergence, $F(t) = t \log t$

$$\begin{aligned}\mathcal{L}_{\text{KL}}^{\text{fw}} &= \left\langle \frac{f(x)}{q(x)} \log \frac{f(x)}{g_\theta(x)} \right\rangle_{x \sim q(x)} \\ \mathcal{L}_{\text{KL}}^{\text{inv}} &= \left\langle \frac{f(\bar{G}_\theta(z))}{\bar{g}_\theta(z)} \log \frac{f(\bar{G}_\theta(z))}{\bar{g}_\theta(z)} \right\rangle_{z \sim p_0(z)}.\end{aligned}\quad (28)$$

- reverse KL-divergence, $F(t) = -\log t$

$$\begin{aligned}\mathcal{L}_{\text{RKL}}^{\text{fw}} &= \left\langle \frac{g_\theta(x)}{q(x)} \log \frac{g_\theta(x)}{f(x)} \right\rangle_{x \sim q(x)} \\ \mathcal{L}_{\text{RKL}}^{\text{inv}} &= \left\langle \log \frac{\bar{g}_\theta(z)}{f(\bar{G}_\theta(z))} \right\rangle_{z \sim p_0(z)}.\end{aligned}\quad (29)$$

We can test these six scenarios of forward and inverse training using three different divergences on triple-W production. To this end, we run a simple single-channel MADNIS training without buffered training, with the hyperparameters given in Tab. 2. We estimate the stability of the training and results by repeating each training ten times. In Fig. 1, we first show the training behavior for the different scenarios. We immediately see that the KL-divergence leads to the most stable training. In contrast, the RKL-divergence combined with inverse training is the most noisy. In terms of performance measured by the final loss value, forward training consistently beats inverse training.

In Fig. 2, we show the unweighting efficiencies and the standard deviations of the integral as more quantitative quality measures. For the standard deviation, we see that variance and

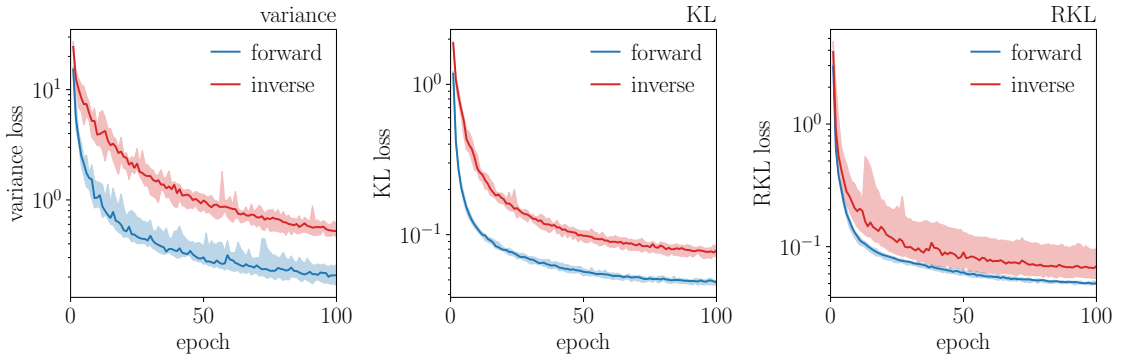


Figure 1: Loss values as a function of the training epochs for different losses: variance, KL-divergence, and RKL-divergence from left to right.

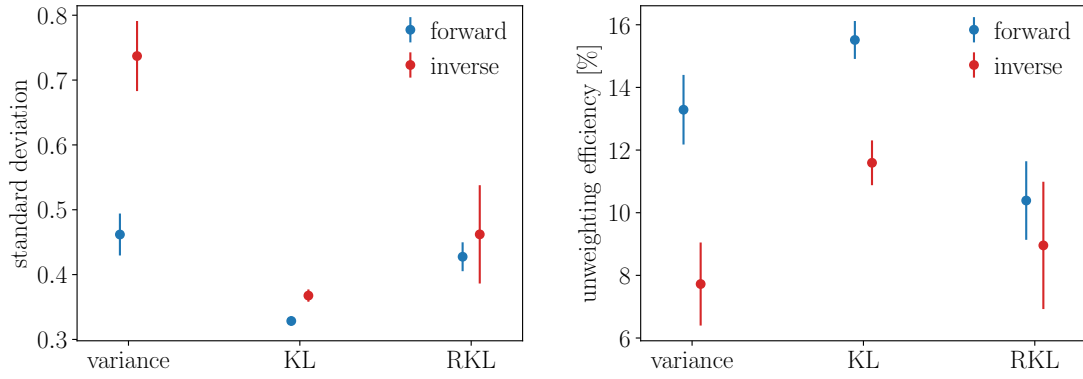


Figure 2: Relative standard deviations (left) and unweighting efficiencies (right) for different loss functions.

RKL losses used for forward training lead to similar results, but the KL-divergence outperforms them. Also, in terms of unweighting efficiency, forward training with a KL-loss leads to the best results. The fact that RKL gives the worst unweighting efficiency is related to overweights, which the RKL does not penalize. This comparison has to be taken with a grain of salt, because the performance of forward training based on the variance and the KL-divergence are close in performance. An additional aspect we have to factor in is that a multi-channel loss can only be constructed using the variance, whereas the KL-divergence might be most suitable for single-channel integrals.

Additional derivatives

When using differentiable integrands, we can also evaluate an additional derivative matching term (also called score or force matching [99]) for each forward loss introduced above,

$$\mathcal{L}^{\text{fw}} \rightarrow \mathcal{L}^{\text{fw}} + \lambda \langle |\partial_x \log f(x) - \partial_x \log g_\theta(x)|^2 \rangle_{x \sim q(x)}. \quad (30)$$

The relative strength of the derivative term, λ , is a hyperparameter. In Fig. 3, we show the same triple-W results as in Fig. 2, but including derivative matching with different strengths λ . For the variance and RKL losses, we see slight improvements in the results from the derivative matching. However, it turns out that it comes with less stable training. Altogether, the

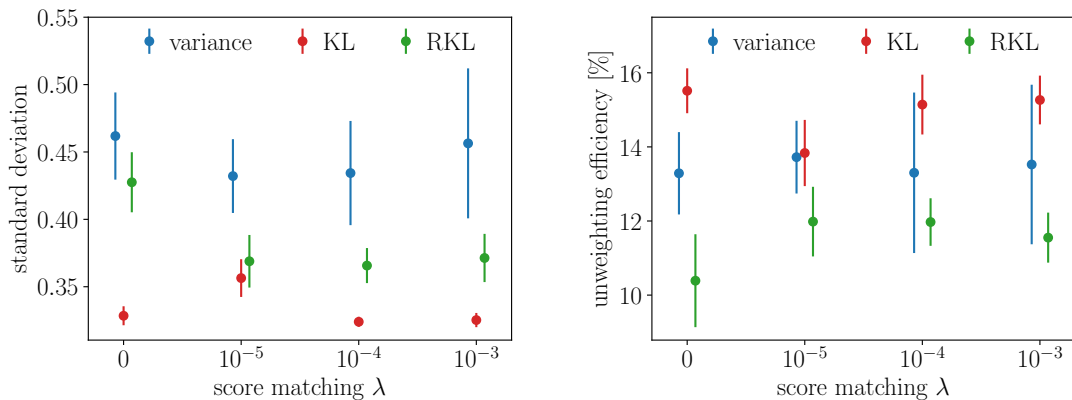


Figure 3: Relative standard deviations (left) and unweighting efficiencies (right) for different derivative matching coefficients.

improvements from adding the derivative are relatively small, leading to the non-trivial question if their performance gain justifies the additional computational cost from evaluating the gradients. Moreover, generalizing this additional term to buffered training for multi-channel integration would come with a very large memory footprint.

4 Differentiable phase space — MADNIS-Lite

To define differentiable and trainable phase-space mappings, we re-introduce the relevant building blocks using consistent notation. For a hadron-collider process

$$p_1 + p_2 \rightarrow k_1 + \dots + k_n \quad (31)$$

the differential cross section is given by

$$d\sigma = \sum_{a,b} dx_1 dx_2 d\Phi^{2 \rightarrow n} f_a(x_1) f_b(x_2) \frac{(2\pi)^{4-3n}}{2x_1 x_2 s} |\mathcal{M}_{ab}(p_1, p_2 | k_1, \dots, k_n)|^2, \quad (32)$$

with a sum over initial-state partons and the phase space density

$$d\Phi^{2 \rightarrow n} = \left[\prod_{i=1}^n d^4 k_i \delta(k_i) \theta(k_i^0) \right] \delta^{(4)} \left(p_1 + p_2 - \sum_i k_i \right). \quad (33)$$

The total cross section is

$$\begin{aligned} \sigma &= \int dx_1 dx_2 d\Phi^{2 \rightarrow n}(x) f(x) \equiv \int dx f(x) \\ &\text{with } f(x) = \frac{(2\pi)^{4-3n}}{2x_1 x_2 s} \sum_{a,b} f_a(x_1) f_b(x_2) |\mathcal{M}_{ab}(x)|^2, \end{aligned} \quad (34)$$

in terms of the phase space vector $x = (x_1, x_2, k_i)$.

4.1 Parameterized mappings

For a single channel, we choose a suitable mapping of x to a unit-hypercube z ,

$$\sigma = \int dx f(x) = \int dz \frac{f(x)}{g(x)} \Big|_{x=\bar{G}(z)} \quad (35)$$

To minimize the integration error, we choose the mapping g to follow the peaking propagator structure of $f(x)$, as encoded in the Feynman diagrams. To this end, we decompose the phase-space integral into integrals over time-like invariants s_i , $2 \rightarrow 2$ scattering processes with t -channel propagators, and $1 \rightarrow 2$ particle decays,

$$\int d\Phi^{2 \rightarrow n}(x) = \prod_{i=1}^{n-2} \int_{s_{i,\min}}^{s_{i,\max}} ds_i \prod_{j=1}^{\kappa} \int d\Phi_j^{2 \rightarrow 2}(x) \prod_{k=1}^{n-\kappa-1} \int d\Phi_k^{1 \rightarrow 2}(x). \quad (36)$$

The number of $2 \rightarrow 2$ processes and $1 \rightarrow 2$ decays depends on the diagram the mapping is based on. If several t -channel propagators are present, i.e. for $\kappa \geq 2$, some of the s_i do not correspond to propagators in the diagram and they are sampled uniformly. For the $(3n - 4)$ -dimensional integral this results in

- $d_s = n - 2$ degrees of freedom from time-like invariants;
- $d_p = 2\kappa$ degrees of freedom from $2 \rightarrow 2$ scatterings.
- $d_d = 2(n - \kappa - 1)$ degrees of freedom from decays;

Together with the PDF convolutions, this covers $3n - 2$ integral dimensions. For each of these sub-integrals, it is possible to define appropriate mappings $x \leftrightarrow z$ as it is commonly done in many multi-purpose event generators [1–3]. We implement these physics-inspired mappings in a differentiable and invertible way using PYTORCH, allowing us to perform forward training. In the following, we briefly review our parametrization [122] for each phase-space block needed to understand how they can be upgraded by additional trainable transformations.

Propagator invariants

To construct a smooth mapping for a propagator

$$|\mathcal{M}|^2 \propto \frac{1}{(s - M^2)^2 + M^2\Gamma^2}, \quad (37)$$

we map the invariant s to a random number $z_s = G_{\text{prop}}(s)$ such that

$$\int_{s_{\min}}^{s_{\max}} ds = \int_0^1 \frac{dz}{g_{\text{prop}}(s(z_s), s_{\min}, s_{\max})} = \int_0^1 dz \left| \frac{\partial \bar{G}_{\text{prop}}(z_s, m^2, s_{\min}, s_{\max})}{\partial z} \right|. \quad (38)$$

Depending on the propagator width, we can introduce two different mappings. For a Breit-Wigner propagator we use

$$\begin{aligned} \bar{G}_{\text{prop}}^{\text{BW}}(z_s, m^2, s_{\min}, s_{\max}) &= m\Gamma \tan[y_1 + (y_2 - y_1)z_s] + m^2 \\ g_{\text{prop}}^{\text{BW}}(s, m^2, s_{\min}, s_{\max}) &= \frac{m\Gamma}{(y_2 - y_1)[(s - m^2)^2 + m^2\Gamma^2]} \\ y_{1/2} &= \arctan\left(\frac{s_{\min/\max} - m^2}{m\Gamma}\right). \end{aligned} \quad (39)$$

For $\Gamma = 0$ we instead employ

$$\begin{aligned} \bar{G}_{\text{prop}}^\nu(z_s, m^2, s_{\min}, s_{\max}) &= [z_s(s_{\max} - m^2)^{1-\nu} + (1 - z_s)(s_{\min} - m^2)^{1-\nu}]^{\frac{1}{1-\nu}} + m^2 \\ g_{\text{prop}}^\nu(s, m^2, s_{\min}, s_{\max}) &= \frac{1 - \nu}{[(s_{\max} - m^2)^{1-\nu} - (s_{\min} - m^2)^{1-\nu}](s - m^2)^\nu}, \end{aligned} \quad (40)$$

as long as $\nu \neq 1$. The parameter ν can be tuned, and the naive expectation $\nu = 2$ is not necessarily the best choice. We choose $\nu = 1.4$ and then optimize the mapping as explained below.

2 \rightarrow 2 scattering processes

For a $2 \rightarrow 2$ scattering with $p_1 + p_2 = k_1 + k_2$, the momenta $p_{1,2}$ and the virtualities k_i^2 are fixed or sampled from other phase-space components. As this includes a t -channel propagator, we

choose

$$\begin{aligned} \int d\Phi^{2\rightarrow 2}(p_1, p_2; k_1^2, k_2^2) &= \frac{1}{4\sqrt{\lambda(p^2, p_1^2, p_2^2)}} \int_0^{2\pi} d\phi^* \int_{-t_{\max}}^{-t_{\min}} d|t| \\ &= \int_0^1 \frac{dz_\phi dz_t}{g_{2\rightarrow 2}(p^2, p_1^2, p_2^2, t, m^2, \nu, t_{\min}, t_{\max})}, \end{aligned} \quad (41)$$

where ϕ^* is the azimuthal angle defined by p_1 and k_1 in the CM frame of $p = p_1 + p_2$, and $\lambda(x, y, z) = (x - y - z)^2 - 4yz$. The invariant $t = (p_1 - k_1)^2 < 0$ depends only linearly on the azimuthal angle $\cos \theta^*$ as

$$t = k_1^2 + p_1^2 - \frac{(p^2 + k_1^2 - k_2^2)(p^2 + p_1^2 - p_2^2) - \sqrt{\lambda(p^2, k_1^2, k_2^2)}\sqrt{\lambda(p^2, p_1^2, p_2^2)} \cos \theta^*}{2p^2}. \quad (42)$$

The integration boundaries can be calculated from this with $-1 \leq \cos \theta^* \leq 1$. We sample the polar angle and t according to

$$\phi^* = 2\pi z_\phi \quad \text{and} \quad |t| = \bar{G}_{\text{prop}}^\nu(z_t, m^2, -t_{\max}, -t_{\min}), \quad (43)$$

with, correspondingly,

$$g_{2\rightarrow 2}(p^2, p_1^2, p_2^2, t, m^2, \nu, t_{\min}, t_{\max}) = \frac{2}{\pi} \sqrt{\lambda(p^2, p_1^2, p_2^2)} g_{\text{prop}}(-t, m^2, \nu, -t_{\max}, -t_{\min}). \quad (44)$$

Further, for each t -channel block in our diagram, the corresponding s -invariant, i.e. $p^2 = s$, also needs to be sampled as time-like invariant in Eq.(36). However, in contrast to invariants reflecting propagators in the diagram, these invariants belong to pseudo particles and can be sampled flat

$$\begin{aligned} \bar{G}_{\text{pseudo}}(z_s, s_{\min}, s_{\max}) &= z_s (s_{\max} - s_{\min}) + s_{\min} \\ g_{\text{pseudo}}(s, s_{\min}, s_{\max}) &= \frac{1}{s_{\max} - s_{\min}}. \end{aligned} \quad (45)$$

1 \rightarrow 2 particle decays

For isotropic decays with $p = k_1 + k_2$, the momentum p and the virtualities k_i^2 are again sampled from other phase-space components. We choose the polar angle ϕ^* and azimuthal angle θ^* in the decay rest frame as integration variables and sample $\phi^* = 2\pi z_\phi$ and $\cos \theta^* = 2z_\theta - 1$ uniformly,

$$\begin{aligned} \int d\Phi^{1\rightarrow 2}(p; k_1^2, k_2^2) &= \frac{\sqrt{\lambda(p^2, k_1^2, k_2^2)}}{8p^2} \int_0^{2\pi} d\phi^* \int_{-1}^1 d\cos \theta^* = \frac{1}{g_{\text{decay}}(p^2, k_1^2, k_2^2)} \int_0^1 dz_1 dz_2 \\ &\text{with} \quad g_{\text{decay}}(p^2, k_1^2, k_2^2) = \frac{2p^2}{\pi \sqrt{\lambda(p^2, k_1^2, k_2^2)}}. \end{aligned} \quad (46)$$

PDF convolutions

For the PDF convolutions, we introduce $\tau = x_1 x_2$, such that the squared partonic CM energy is given by $\hat{s} = \tau s$. This allows us to write

$$\int_0^1 dx_1 dx_2 \Theta(\hat{s} - \hat{s}_{\min}) = \int_{\tau_{\min}}^1 d\tau \int_{\tau}^1 \frac{dx_1}{x_1} = \int_0^1 \frac{dz_{\tau} dz_{x_1}}{g_{\text{lumi}}(\tau, \tau_{\min})} \quad (47)$$

with $g_{\text{lumi}}(\tau, \tau_{\min}) = \frac{1}{\tau \log \tau \log \tau_{\min}}$,

where \hat{s}_{\min} follows from final-state masses and cuts and we sample

$$\tau = \tau_{\min}^{1-z_{\tau}} \quad \text{and} \quad x_1 = \tau^{z_{x_1}}. \quad (48)$$

The induced density g_{lumi} exactly cancels the flux factor τ^{-1} in Eq.(32). If there are no t -channels, i.e. $\kappa = 0$, the squared CM energy \hat{s} also belongs to a propagator in the diagram. In this case, it is beneficial to sample τ such that this propagator structure is mapped out.

Each of the s -invariants, $2 \rightarrow 2$ scatterings, and decay blocks described above transform one or two random numbers. They can appear multiple times for a given Feynman diagram, as illustrated in Fig. 4. In Appendix C, we illustrate how these components are combined to parametrize a complete channel mapping for $W + 4$ jets production.

4.2 Learnable bilinear spline flows

For typical a MADNIS training, the flow sub-networks often encode relatively simple functions. For these cases, we introduce bilinear spline flows to replace the sub-networks with second-order polynomials. A d_x -dimensional transformation $x \leftrightarrow z$ with a d_c -dimensional condition

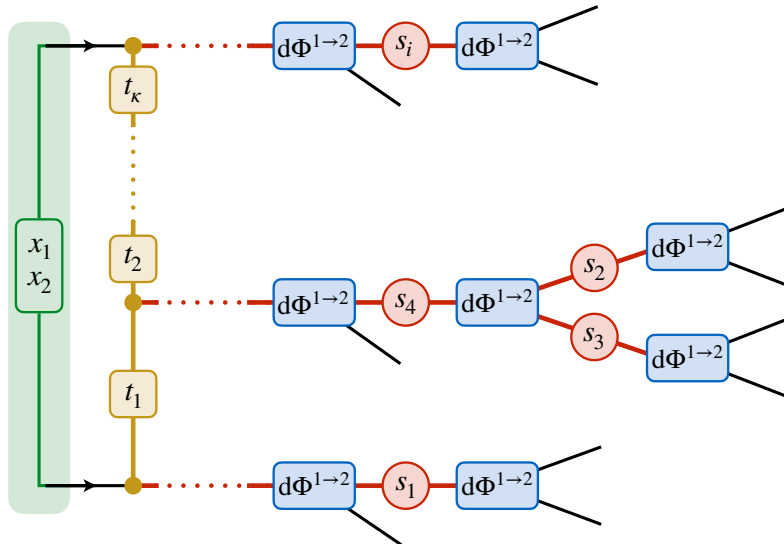


Figure 4: Topological diagram illustrating our separable and differentiable phase-space mappings. Each colored block represents one of the introduced components which can be modified by a trainable bilinear flow.

c can be written as

$$z = G(x; W\hat{c}) \quad \text{with} \quad \hat{c} = \begin{pmatrix} 1 \\ c_i \\ c_i c_j \end{pmatrix} \quad \text{for } i \leq j, \quad (49)$$

where G is a rational quadratic spline transformation and W is a trainable matrix. The number of trainable parameters for such a transformation with n_b bins is

$$d_W = (3n_b + 1) \times d_x \times \left(1 + d_c + \frac{1}{2}d_c(d_c + 1) \right). \quad (50)$$

This way, we can build small and fast, but sufficiently expressive trainable transformations for a small number of dimensions d_x and d_c . Another benefit is the interpretability of bilinear spline flows because W tells us how strongly the spline transformation is correlated with the conditional inputs.

We can combine these trainable mappings with the propagator, decay, scattering, and PDF blocks introduced above and use them to transform their uniform random number input. For mappings with two random numbers, we allow for correlations between the two dimensions. Because all parts of the phase-space mappings are differentiable, the bilinear flow can even be conditional on intermediate physical features that are available only during the evaluation of the phase-space mapping. This enhances the expressivity and interpretability of the learned transformation.

Implementation

We implement the trainable bilinear spline flows with 6 spline bins. We list the trainable components of the phase space mappings, the conditional features, and the number of trainable parameters in Tab. 1. These parameters are shared between channels and multiple instances of the same block in one channel. This way, the number of trainable parameters stays the same for different processes and allows the use of mappings trained on one process, like $W + 3$ jets,

Mapping	Parameters	Conditions
Time-like invariants, Eqs.(39),(40) (separate for massless and massive propagators)	190	partonic CM energy $\sqrt{\hat{s}/s_{\text{lab}}}$ minimal decay CM energy $\sqrt{s_{\text{min}}/s_{\text{lab}}}$ maximal decay CM energy $\sqrt{s_{\text{max}}/s_{\text{lab}}}$
$2 \rightarrow 2$ scattering, Eq.(43)	798	correlations between z_t, z_ϕ partonic CM energy $\sqrt{\hat{s}/s_{\text{lab}}}$ scattering CM energy $\sqrt{p^2/s_{\text{lab}}}$ virtualities $\sqrt{k_{1,2}^2/s_{\text{lab}}}$
Time-like invariants for pseudo-particles, Eq.(45)	190	partonic CM energy $\sqrt{\hat{s}/s_{\text{lab}}}$ minimal energy $\sqrt{s_{\text{min}}/s_{\text{lab}}}$ maximal energy $\sqrt{s_{\text{max}}/s_{\text{lab}}}$
$1 \rightarrow 2$ decay, Eq.(46)	380	correlations between z_θ, z_ϕ partonic CM energy $\sqrt{\hat{s}/s_{\text{lab}}}$ decay CM energy $\sqrt{p^2/s_{\text{lab}}}$
PDF convolutions, Eq.(48)	114	correlations between z_τ, z_{x_1}

Table 1: Trainable components

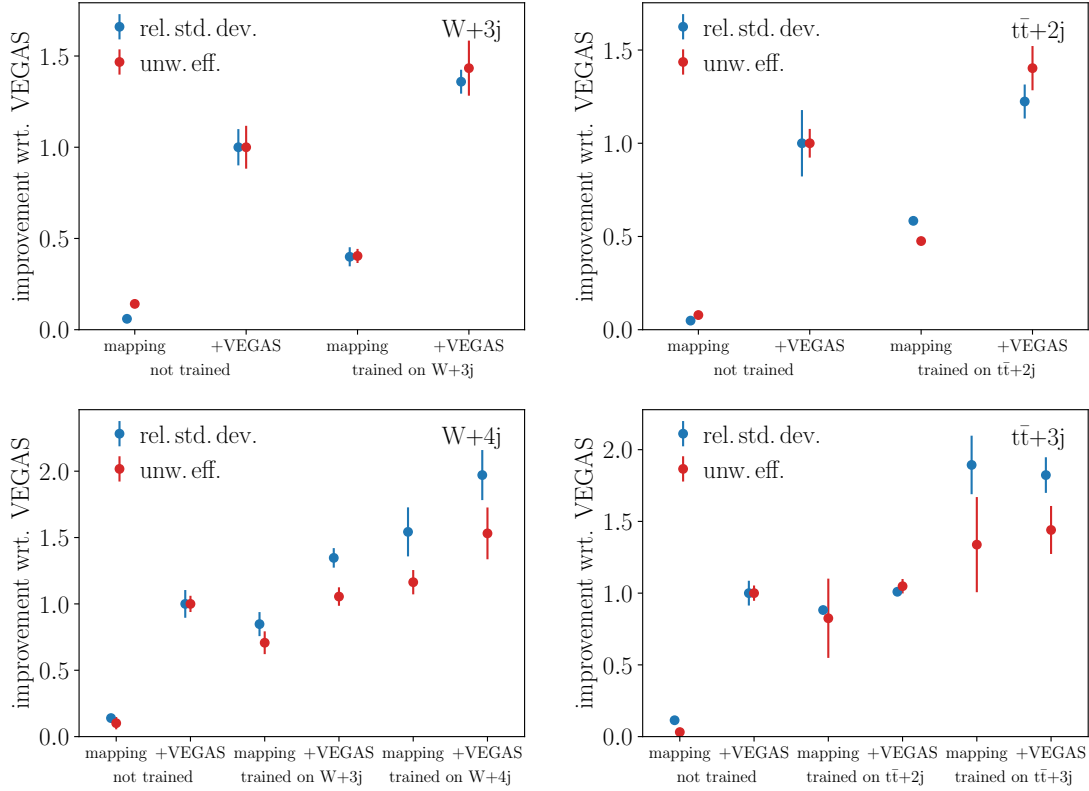


Figure 5: Improvement of the unweighting efficiency and relative standard deviation of different setups with respect to an untrained phase space mapping refined with VEGAS for W +jets (left) and $t\bar{t}$ +jets (right).

for reasonably related other processes. Note that for processes like $W + 4$ jets ($t\bar{t} + 3$ jets) with up to 384 (945) integration channels, this parameter sharing reduces the computational cost significantly.

We train MADNIS-Lite using the multi-channel variance loss from Eq.(14), but without trainable channel weights. We use stratified training to focus the available training samples on channels with a large contribution to the total cross section, and buffered training to reduce the number of integrand evaluations. The training hyperparameters are given in Tab. 3.

Performance

In Fig. 5, we compare the unweighting efficiencies and relative integration errors for different scenarios and different processes. Throughout all considered processes, we benchmark our trained mappings against the raw mappings combined with and without VEGAS. The shown error bars were obtained by running the integration, including VEGAS optimization if applicable, ten times and taking the mean and standard deviation. All results are shown relative to the VEGAS performance without trained mappings.

We start by considering the $W + 3$ jets process in the upper left plot of Fig. 5. The trained mappings without additional VEGAS optimization outperform the raw phase-space mapping but are a bit worse than the VEGAS optimized mappings. This is because the number of trainable parameters of our bilinear flow is quite small as it is shared among multiple channels and building blocks, see Tab. 1. In contrast, VEGAS builds an independent grid for each channel and phase-space direction, resulting in more than 30k optimized parameters. When combining

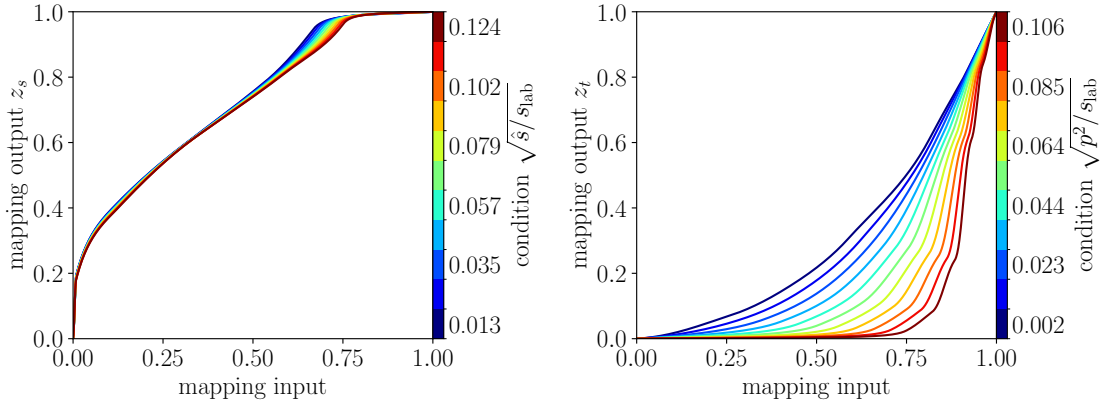


Figure 6: Mappings learned by the bilinear spline flow for $W+3$ jets. Left panel: Learned mapping for the time-like invariant for massless propagators, conditional on the partonic CM energy $\sqrt{\hat{s}}$. Right panel: Learned mapping for the t -invariant in $2 \rightarrow 2$ scatterings, conditional on the scattering CM energy $\sqrt{p^2}$.

our trained mapping with VEGAS, we achieve the best performance in the $W + 3$ jets scenario, with an improvement factor of up to 1.5. For the $t\bar{t} + 2$ jets scenario in the upper right plot, the story is the same.

Next, we consider the same processes but with an additional jet in the final state. The results for different scenarios are shown in the lower two plots in Fig. 5. Again, we consider the mapping that has been trained on the $W+3$ jets process and evaluate it on the $W+4$ jets process without further training. We find that the pre-trained mappings are very close in performance to the VEGAS benchmark, without any specific optimization on the $W + 4$ jets process. Like before, when additionally combining with VEGAS we outperform our untrained phase-space mappings. If we directly train our mappings on $W + 4$ jets, we immediately outperform our untrained benchmark mappings even without further optimizing with VEGAS. When combining the trained mappings with an additional VEGAS optimization, we achieve an improvement factor of up to 2 for the $W + 4$ jets process.

Again, when turning to the $t\bar{t} + 3$ jets scenario, we observe the same behavior. This indicates that our trainable mappings work well and are capable of generalizing from one process to another process with an additional final state jet. This means our trainable bilinear flow represents the smallest foundation model possible. We note that going even one step further by pre-training our bilinear flows on $W + 2$ jets and $t\bar{t} + 1$ jets, respectively, does not generalize well to higher multiplicities as these low-multiplicity processes are too simple to encode all the necessary information.

Explainability

Another benefit of using our bilinear-flow-enhanced mappings is the possibility to understand and interpret the learned correlations. As an example, we consider the learned transformation for the $W+3$ jets process in Fig. 6. Both plots show a learned transformation of an input of one of the phase-space blocks conditional on some physical features relevant to that component. In the left panel of Fig. 6, we consider the learned transformation for a massless propagator conditional on the partonic CM energy $\sqrt{\hat{s}}$. We can see that the overall shape of the mapping deviates from the flat mapping, being slightly bulged upwards. This means that our fixed choice of $\nu = 1.4$ was slightly too large, indicating stronger pole cancellations in the collinear limit. Further, the mapping tends to avoid $z_s < 0.2$ and hence avoiding to sample the s_{\min}

region due to p_T cuts on the final state jets. In contrast, the mapping favors sampling into $s \approx s_{\max}$ stemming from momentum conservation in dominating integration channels containing only s -channels. This means, we possibly need to allow for a more flexible optimization of the time-like invariants depending on the underlying topology or the linked particle id. On top of this overall correlation, we can also look into the dependence on the $\sqrt{\hat{s}}$. The condition is varied between 2.5% and 97.5% of the quantile from the distribution of values that this block sees during event generation. We can observe that varying $\sqrt{\hat{s}}$ only has a very small effect on the mapping of the s -invariant, indicating a small correlation.

For the right panel of Fig. 6, we consider the learned mapping for the t -invariant in a $2 \rightarrow 2$ scattering block conditioned on the CM energy $\sqrt{p^2}$ of that $2 \rightarrow 2$ scattering. In this case, varying $\sqrt{p^2}$ has a large influence on the optimal t -invariant mapping. This means that for larger p^2 , the mapping tends to sample smaller z_t , which is physically linked to smaller scattering angles θ^* in the center-of-mass system of the $2 \rightarrow 2$ scattering block and thus prefers very forward scattering.

5 Outlook

Modern machine learning is a promising path to improve the critical multi-purpose event generators to the speed and precision level required by the HL-LHC. For MADGRAPH, the MADNIS [6, 7] project has shown that significant gains can be realized by implementing multi-channel importance sampling using modern neural networks.

An exciting and equally promising new approach is differentiable programming applied to event generation [99]. We have tested the potential gains from a differentiable MADNIS for two setups. First, we have developed a fully differentiable combination of matrix element, phase space, and parton densities to use derivative information for optimal integration and sampling. While this setup works well, we have not found significant improvements over the established MADNIS methodology.

As a second and more lightweight use of differentiable code, we have developed a new, modular, and differentiable phase-space mapping. This MADNIS-Lite approach factorizes the phase space into differentiable standard blocks, each consisting of a physics-inspired mapping and a learnable bilinear spline flow. These blocks have the great advantage of being economical and generalizable, so they are much easier to train and use than the full MADNIS framework. For a set of benchmark processes, they show great promise and low computational cost.

Altogether, this allows us to combine three strategies for future MADGRAPH releases: (i) the standard multi-channel importance sampling using VEGAS techniques provides fast results whenever the integrand factorizes at least approximately; (ii) for more complex Feynman diagrams with factorizing physics structures, which might not be easily mapped on individual phase space directions, MADNIS-Lite provides efficient and fast ML-integration and sampling; (iii) for the highest precision and general matrix elements, including, for instance, gauge cancellations between Feynman diagrams, MADNIS leads to significant improvements over established methods. In combination, these methods provide the ML backbone for optimal event generation at the HL-LHC.

Acknowledgements

First, we would like to thank Michael Kagan and Lukas Heinrich for continuous encouragement by asking all the right questions many times. OM and RW acknowledge support by FRS-FNRS (Belgian National Scientific Research Fund) IISN projects 4.4503.16. TP and TH

are supported by the Deutsche Forschungsgemeinschaft (DFG, German Research Foundation) under grant 396021762 – TRR 257 *Particle Physics Phenomenology after the Higgs Discovery*. TH is funded by the Carl-Zeiss-Stiftung through the project *Model-Based AI: Physical Models and Deep Learning for Imaging and Cancer Treatment*. The authors acknowledge support by the state of Baden-Württemberg through bwHPC and the German Research Foundation (DFG) through grant no INST 39/963-1 FUGG (bwForCluster NEMO).

A Hyperparameters

Parameter	Value
Optimizer	Adam [123]
Learning rate	0.001
LR schedule	exponential
Final learning rate	0.0001
Batch size	1024
Training length	10k batches
Permutations	Logarithmic decomposition [18]
Number of coupling blocks	$2 \lceil \log_2 D \rceil = 6$
Coupling transformation	RQ splines [124]
Subnet hidden nodes	32
Subnet depth	3
Activation function	leaky ReLU

Table 2: MADNIS hyperparameters used in Sec. 3.

Parameter	Value
Optimizer	Adam
Learning rate	0.01
LR schedule	exponential
Final learning rate	0.001
Batch size	$\min(200 \cdot n_c^{0.8}, 10000)$
Buffered training gain [6]	6
Training length	7.8k batches
Uniform training fraction [7]	0.1
RQ spline bins	6
VEGAS iterations	7
VEGAS bins	64
VEGAS samples per iteration	20k
VEGAS damping α	0.7

Table 3: MADNIS-Lite and VEGAS hyperparameters used in Sec. 4.

B Analytic loss function gradients

To exemplify the properties of the forward and inverse loss, we consider a simple 1-dimensional target function f as

$$f(x) = \frac{1}{\sqrt{2\pi}} \exp\left(-\frac{x^2}{2}\right). \quad (51)$$

The latent distribution is given as a standard normal distribution as

$$p_0(z) = \frac{1}{\sqrt{2\pi}} \exp\left(-\frac{z^2}{2}\right). \quad (52)$$

We now assume a simple trainable mapping (1D flow if you want), given by

$$x \equiv \bar{G}_\theta(z) = \theta \cdot z \quad \longleftrightarrow \quad z \equiv G_\theta(x) = \frac{z}{\theta}. \quad (53)$$

inducing the Jacobian determinants

$$\left| \frac{\partial G_\theta(x)}{\partial x} \right| = \frac{1}{\theta} \longleftrightarrow \left| \frac{\partial \bar{G}_\theta(z)}{\partial z} \right| = \theta. \quad (54)$$

Combining this with the prior sample density yields the overall importance sampling (pseudo) density

$$g_\theta(x) = p_0(G_\theta(x)) \left| \frac{\partial G_\theta(x)}{\partial x} \right| = \frac{1}{\sqrt{2\pi\theta^2}} \exp\left(-\frac{x^2}{2\theta^2}\right) \quad (55)$$

$$\bar{g}_\theta(z) = p_0(z) \left| \frac{\partial \bar{G}_\theta(z)}{\partial z} \right|^{-1} = \frac{1}{\sqrt{2\pi\theta^2}} \exp\left(-\frac{z^2}{2}\right) \quad \text{with } \bar{g}_\theta(G_\theta(x)) = g_\theta(x). \quad (56)$$

In this case, the integral of f can be calculated as

$$I = \int dx f(x) = \int dx g_\theta(x) \frac{f(x)}{g_\theta(x)} = \left\langle \frac{g_\theta(x)}{q(x)} \frac{f(x)}{g_\theta(x)} \right\rangle_{x \sim q(x)} = 1. \quad (57)$$

Variance loss

While the integral does not change, the variance of the integrand is given by

$$\begin{aligned} \mathcal{L}_{\text{inv}}^{\text{fw}} = \mathcal{L}_{\text{var}}^{\text{inv}} &= \left\langle \frac{g_\theta(x)}{q(x)} \left(\frac{f(x)}{g_\theta(x)} - 1 \right)^2 \right\rangle_{x \sim q(x)} \\ &= \int dx g_\theta(x) \left(\frac{f(x)}{g_\theta(x)} - 1 \right)^2 \\ &= \frac{\theta^2}{\sqrt{2\theta^2 - 1}} - 1 \quad \text{for } \theta > \frac{1}{\sqrt{2}}, \end{aligned} \quad (58)$$

which is exactly zero for the expected value of $\theta = 1$. Next, we can calculate the expectation value of the gradient of the integrand with respect to θ , as this quantity is used during optimization. This yields

$$\nabla_\theta \mathcal{L}_{\text{var}}^{\text{fw}} = \nabla_\theta \mathcal{L}_{\text{var}}^{\text{inv}} = \frac{2\theta(\theta^2 - 1)}{(2\theta^2 - 1)^{3/2}}. \quad (59)$$

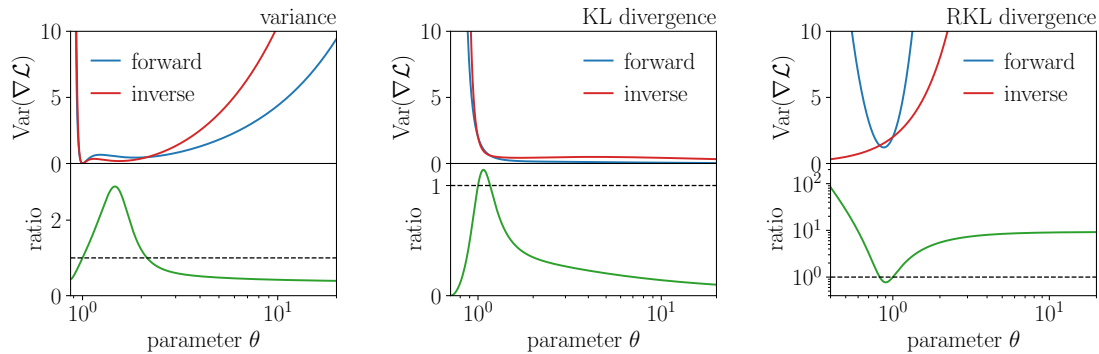


Figure 7: Analytic solutions for the variance of the gradients of different loss functions

On the other hand, the variance of the gradient is given by

$$\begin{aligned}
\text{Var}_{x \sim q(x)} &= \left\langle \left(\nabla_{\theta} \frac{g_{\theta}(x)}{q(x)} \left(\frac{f(x)}{g_{\theta}(x)} - 1 \right)^2 - \nabla_{\theta} \mathcal{L}_{\text{var}}^{\text{fw}} \right)^2 \right\rangle_{x \sim q(x)} \\
&= \int dx q(x) \left(\nabla_{\theta} \frac{g_{\theta}(x)}{q(x)} \left(\frac{f(x)}{g_{\theta}(x)} - 1 \right)^2 - \nabla_{\theta} \mathcal{L}_{\text{var}}^{\text{fw}} \right)^2 \\
&= -\frac{1}{4} \left(2 - \frac{8}{\theta^2} - \frac{2}{(2\theta^2 - 1)^2} + \frac{2}{(2\theta^2 - 1)^3} + \frac{24}{(2\theta^2 - 1)^{5/2}} \right. \\
&\quad - \frac{16}{(2\theta^2 - 1)^{3/2}} - \frac{2}{2\theta^2 - 1} + \frac{8}{(2\theta^2 - 1)^{1/2}} \\
&\quad \left. - \frac{9}{(4\theta^2 - 3)^{5/2}} + \frac{3}{(4\theta^2 - 3)^{3/2}} - \frac{1}{(4\theta^2 - 3)^{1/2}} - \sqrt{4\theta^2 - 3} \right). \tag{60}
\end{aligned}$$

However, for the inverse training, we obtain the variance of the gradient as

$$\begin{aligned}
\text{Var}_{z \sim p_0(z)} &= \left\langle \left(\nabla_{\theta} \left(\frac{f(\bar{G}_{\theta}(z))}{\bar{g}_{\theta}(z)} - 1 \right)^2 - \nabla_{\theta} \mathcal{L}_{\text{var}}^{\text{inv}} \right)^2 \right\rangle_{z \sim p_0(z)} \\
&= \int dz p_0(z) \left(\nabla_{\theta} \left(\frac{f(\bar{G}_{\theta}(z))}{\bar{g}_{\theta}(z)} - 1 \right)^2 - \nabla_{\theta} \mathcal{L}_{\text{var}}^{\text{inv}} \right)^2 \\
&= -\frac{1}{16} \left(8 - \frac{8}{(2\theta^2 - 1)^2} + \frac{8}{(2\theta^2 - 1)^3} - \frac{48}{(2\theta^2 - 1)^{5/2}} \right. \\
&\quad - \frac{32}{(2\theta^2 - 1)^{3/2}} - \frac{8}{2\theta^2 - 1} - \frac{48}{(2\theta^2 - 1)^{1/2}} \\
&\quad - \frac{81}{(4\theta^2 - 3)^{5/2}} - \frac{9}{(4\theta^2 - 3)^{3/2}} - \frac{27}{(4\theta^2 - 3)^{1/2}} \\
&\quad \left. - 11\sqrt{4\theta^2 - 3} + \frac{256\theta(3\theta^4 - 4\theta^2 + 2)}{(3\theta^2 - 2)^{5/2}} \right). \tag{61}
\end{aligned}$$

KL loss

For the expectation value of the gradient, we obtain for both directions

$$\nabla_{\theta} \mathcal{L}_{\text{KL}}^{\text{fw}} = \nabla_{\theta} \mathcal{L}_{\text{KL}}^{\text{inv}} = \frac{\theta^2 - 1}{\theta^3}. \tag{62}$$

While for the variance, we obtain

$$\text{Var}(\nabla_{\theta} \mathcal{L}_{\text{KL}}^{\text{fw}}) = -\frac{1}{\theta^6} + \frac{2}{\theta^4} - \frac{1}{\theta^2} + \frac{4\theta^4 - 8\theta^2 + 6}{(2\theta^2 - 1)^{5/2}} \tag{63}$$

$$\begin{aligned}
\text{Var}(\nabla_{\theta} \mathcal{L}_{\text{KL}}^{\text{inv}}) &= \frac{-1}{4\theta^6(2\theta^2 - 1)^{9/2}} \left(\sqrt{2\theta^2 - 1} (4 - 40\theta^2 + 164\theta^4) \right. \\
&\quad - \theta^6 \left[3 + 49\theta^8 + 352\sqrt{2\theta^2 - 1} - 4\theta^6 (27 + 16\sqrt{2\theta^2 - 1}) \right. \\
&\quad \left. \left. + 8\theta^4 (9 + 32\sqrt{2\theta^2 - 1}) - 8\theta^2 (1 + 52\sqrt{2\theta^2 - 1}) \right] \right. \\
&\quad \left. - 4\theta^6 \log(\theta) [1 - 11\theta^2 + 27\theta^4 - 23\theta^6 + 10\theta^8 \right. \\
&\quad \left. + (1 - 2\theta^2)^2 (1 - 2\theta^2 + 3\theta^4) \log(\theta) \right]. \tag{64}
\end{aligned}$$

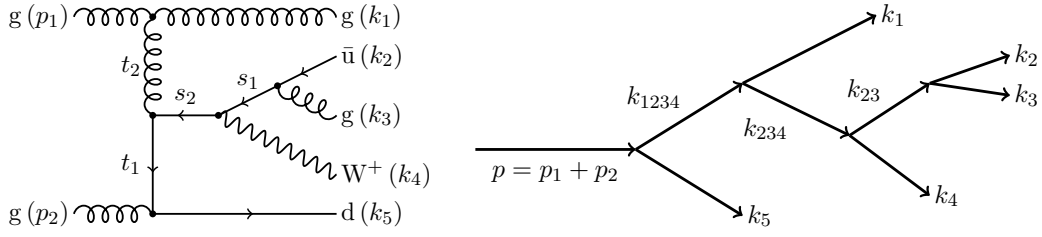


Figure 8: An example Feynman diagram contributing to the $gg \rightarrow W^+ \bar{u} d g g$ process (left) and an illustration of the corresponding phase-space parametrization (right).

RKL Loss

For the expectation value of the gradient, we obtain for both directions

$$\nabla_{\theta} \mathcal{L}_{\text{RKL}}^{\text{fw}} = \nabla_{\theta} \mathcal{L}_{\text{RKL}}^{\text{inv}} = \frac{\theta^2 - 1}{\theta}. \quad (65)$$

While for the variance of the gradient, we obtain

$$\text{Var}(\nabla_{\theta} \mathcal{L}_{\text{RKL}}^{\text{fw}}) = \frac{21 - 54\theta^2 + 37\theta^4 + 4\log(\theta)(3 - 5\theta^2 + \log \theta)}{2\theta^2} \quad (66)$$

$$\text{Var}(\nabla_{\theta} \mathcal{L}_{\text{RKL}}^{\text{inv}}) = 2\theta^2. \quad (67)$$

In Fig. 7, we illustrate the gradient variances for the forward and inverse training for the different loss functions. The upper panels show the absolute gradient variance, while the lower panel shows the ratio between the forward and inverse directions. A ratio of $r > 1$ means the gradient variance of the forward training is larger than the gradient variance of the inverse training. For the variance loss and KL divergence, we can observe that the forward training yields the more stable training. Only in parameter regions around the optimal value, i.e. $\theta \approx \theta_{\text{opt}} = 1$ the inverse training is more stable. In contrast, for the RKL divergence, the picture changes and the inverse loss gives less noisy gradients.

C Explicit channel mapping

As an example, we consider $W + 4$ jets production

$$gg \rightarrow W^+ \bar{u} d g g. \quad (68)$$

In particular, we investigate the Feynman diagram of Fig. 8, because it involves all types of phase-space blocks introduced in Sec. 4. We define

$$\begin{aligned} k_{23} &= k_2 + k_3 & k_{234} &= k_2 + k_3 + k_4 & k_{1234} &= k_1 + k_2 + k_3 + k_4 \\ q_1 &= p_1 - k_1 & q_2 &= p_2 - k_5 & p &= p_1 + p_2. \end{aligned} \quad (69)$$

The infrared and collinear singularities are excluded by a lower cut on $k_{23}^2 > k_{23,\text{min}}^2$. The phase-space integral

$$\begin{aligned} \int d\Phi^{2 \rightarrow 5} |_{\text{Fig.8}} &= \int_{k_{23,\text{min}}^2}^{\hat{s}} dk_{23}^2 \int_{k_{23}^2}^{\hat{s}} dk_{234}^2 \int_{k_{234}^2}^{\hat{s}} dk_{234}^2 \int d\Phi^{2 \rightarrow 2}(p_1, p_2; k_{1234}^2, k_5^2) \\ &\times \int d\Phi^{2 \rightarrow 2}(p_1, q_2; k_1^2, k_{234}^2) \int d\Phi^{1 \rightarrow 2}(k_{234}; k_{23}^2, k_4^2) \int d\Phi^{1 \rightarrow 2}(k_{23}; k_2^2, k_3^2). \end{aligned} \quad (70)$$

is decomposed into two $2 \rightarrow 2$ scattering processes and two decays. The intermediate particles of this decomposition are the virtual particles with momenta k_{23} and k_{234} , and an additional pseudo particle with momentum k_{1234} . First, we perform the luminosity sampling according to Eq.(48) and obtain

$$\begin{aligned} \hat{s} &= s_{\text{lab}}^{z_0} \hat{s}_{\text{min}}^{1-z_0} \quad \text{with} \quad \hat{s}_{\text{min}} = M_W^2 \\ \xi &= \frac{1}{2} \log \frac{x_1}{x_2}, \end{aligned} \quad (71)$$

needed to define $p_{1,2}$ and perform the boost into the proton-proton rest frame. Next, the invariant masses of the external particles of the scattering processes and particle decays have to be determined

$$\begin{aligned} k_{23}^2 &= \overline{G}_{\text{prop}}^{\nu_1}(z_1, 0, k_{23,\text{min}}^2, \hat{s}) \\ k_{234}^2 &= \overline{G}_{\text{prop}}^{\nu_2}(z_2, 0, k_{23}^2, \hat{s}) \\ k_{1234}^2 &= \overline{G}_{\text{prop}}^{\nu=0}(z_3, 0, k_{234}^2, \hat{s}) \equiv z_3(\hat{s} - k_{234}^2) + k_{234}^2. \end{aligned} \quad (72)$$

While the time-like invariants $s_1 = k_{23}^2$ and $s_2 = k_{234}^2$ correspond to massless propagators in the diagram, $s_3 = k_{1234}^2$ is the squared CM energy of the first $2 \rightarrow 2$ scattering (t_1) and belongs to a pseudo particle. Consequently, s_3 is sampled flat. As a next step, the final-state momenta are calculated step-by-step:

- (i) $p_1 + p_2 \rightarrow k_{1234} + k_5$:

The initial-state gluons transform into the final-state d-quark and a pseudo particle with momentum k_{1234} . The invariant mass of the d-quark propagator is given by

$$|q_1^2| = \overline{G}_{\text{prop}}^{\nu_3}(z_4, 0, 0, \hat{s} - k_{1234}^2) \quad (73)$$

where the boundaries are taken from Eq.(42).

- (ii) $p_1 + q_1 \rightarrow k_1 + k_{234}$:

The incoming particles are the initial-state gluon and the incoming virtual d-quark. We further note that $q_1^2 = (p_1 - k_5)^2 = t_1$. The invariant mass of the gluon propagator then reads

$$|q_2^2| = \overline{G}_{\text{prop}}^{\nu_4}(z_5, 0, 0, (k_{1234}^2 - k_{234}^2)(k_{1234}^2 - t_1)/k_{1234}^2) \quad (74)$$

where the boundaries are calculated again from Eq.(42). This fixes the momenta k_1 and k_{234} of the outgoing gluon and the virtual d-quark, respectively.

- (iii) $k_{234} \rightarrow k_{23} + k_4$:

The virtual \bar{d} -quark decays isotropically into the final-state W-boson (k_4) and the virtual \bar{u} -quark (k_{23}).

- (iv) $k_{23} \rightarrow k_2 + k_3$:

Finally, the virtual \bar{u} -quark decays isotropically into the final-state \bar{u} -quark (k_2) and a gluon (k_3).

The total phase-space density is then given by

$$\begin{aligned} g_{\text{tot}} &= g_{\text{lumi}}(\tau, \tau_{\text{min}}) g_{\text{prop}}^{\nu_1}(k_{23}^2, 0, k_{23,\text{min}}^2, \hat{s}) g_{\text{prop}}^{\nu_2}(k_{234}^2, 0, k_{23}^2, \hat{s}) g_{\text{prop}}^{\nu=0}(k_{1234}^2, 0, k_{234}^2, \hat{s}) \\ &\quad \times g_{2 \rightarrow 2}(\hat{s}, 0, 0, t_1, 0, \nu_3, 0, \hat{s} - k_{1234}^2) \\ &\quad \times g_{2 \rightarrow 2}(k_{1234}^2, 0, t_1, t_2, 0, \nu_4, 0, (k_{1234}^2 - k_{234}^2)(k_{1234}^2 - t_1)/k_{1234}^2) \\ &\quad \times g_{\text{decay}}(k_{234}^2, k_{23}^2, 0) g_{\text{decay}}(k_{23}^2, 0, 0) \end{aligned} \quad (75)$$

which includes all propagators of this diagram.

References

- [1] T. Sjöstrand, S. Ask, J. R. Christiansen, R. Corke, N. Desai, P. Ilten, S. Mrenna, S. Prestel, C. O. Rasmussen, and P. Z. Skands, *An introduction to PYTHIA 8.2*, *Comput. Phys. Commun.* **191** (2015) 159, [arXiv:1410.3012 \[hep-ph\]](#).
- [2] J. Alwall, R. Frederix, S. Frixione, V. Hirschi, F. Maltoni, O. Mattelaer, H. S. Shao, T. Stelzer, P. Torrielli, and M. Zaro, *The automated computation of tree-level and next-to-leading order differential cross sections, and their matching to parton shower simulations*, *JHEP* **07** (2014) 079, [arXiv:1405.0301 \[hep-ph\]](#).
- [3] Sherpa Collaboration, *Event Generation with Sherpa 2.2*, *SciPost Phys.* **7** (2019) 3, 034, [arXiv:1905.09127 \[hep-ph\]](#).
- [4] S. Badger *et al.*, *Machine learning and LHC event generation*, *SciPost Phys.* **14** (2023) 4, 079, [arXiv:2203.07460 \[hep-ph\]](#).
- [5] T. Plehn, A. Butter, B. Dillon, T. Heimel, C. Krause, and R. Winterhalder, *Modern Machine Learning for LHC Physicists*, [arXiv:2211.01421 \[hep-ph\]](#).
- [6] T. Heimel, R. Winterhalder, A. Butter, J. Isaacson, C. Krause, F. Maltoni, O. Mattelaer, and T. Plehn, *MadNIS - Neural multi-channel importance sampling*, *SciPost Phys.* **15** (2023) 4, 141, [arXiv:2212.06172 \[hep-ph\]](#).
- [7] T. Heimel, N. Huetsch, F. Maltoni, O. Mattelaer, T. Plehn, and R. Winterhalder, *The MadNIS Reloaded*, *SciPost Phys.* **17** (2024) 023, [arXiv:2311.01548 \[hep-ph\]](#).
- [8] F. Bishara and M. Montull, *Machine learning amplitudes for faster event generation*, *Phys. Rev. D* **107** (2023) 7, L071901, [arXiv:1912.11055 \[hep-ph\]](#).
- [9] S. Badger and J. Bullock, *Using neural networks for efficient evaluation of high multiplicity scattering amplitudes*, *JHEP* **06** (2020) 114, [arXiv:2002.07516 \[hep-ph\]](#).
- [10] J. Aylett-Bullock, S. Badger, and R. Moodie, *Optimising simulations for diphoton production at hadron colliders using amplitude neural networks*, *JHEP* **08** (6, 2021) 066, [arXiv:2106.09474 \[hep-ph\]](#).
- [11] D. Maître and H. Truong, *A factorisation-aware Matrix element emulator*, *JHEP* **11** (2021) 066, [arXiv:2107.06625 \[hep-ph\]](#).
- [12] R. Winterhalder, V. Magerya, E. Villa, S. P. Jones, M. Kerner, A. Butter, G. Heinrich, and T. Plehn, *Targeting multi-loop integrals with neural networks*, *SciPost Phys.* **12** (2022) 4, 129, [arXiv:2112.09145 \[hep-ph\]](#).
- [13] S. Badger, A. Butter, M. Luchmann, S. Pitz, and T. Plehn, *Loop amplitudes from precision networks*, *SciPost Phys. Core* **6** (2023) 034, [arXiv:2206.14831 \[hep-ph\]](#).
- [14] D. Maître and H. Truong, *One-loop matrix element emulation with factorisation awareness*, *JHEP* **5** (2023) 159, [arXiv:2302.04005 \[hep-ph\]](#).
- [15] J. Bendavid, *Efficient Monte Carlo Integration Using Boosted Decision Trees and Generative Deep Neural Networks*, [arXiv:1707.00028 \[hep-ph\]](#).
- [16] M. D. Klimek and M. Perelstein, *Neural Network-Based Approach to Phase Space Integration*, *SciPost Phys.* **9** (2020) 053, [arXiv:1810.11509 \[hep-ph\]](#).

- [17] I.-K. Chen, M. D. Klimek, and M. Perelstein, *Improved neural network Monte Carlo simulation*, *SciPost Phys.* **10** (2021) 1, 023, [arXiv:2009.07819 \[hep-ph\]](#).
- [18] C. Gao, J. Isaacson, and C. Krause, *i-flow: High-dimensional Integration and Sampling with Normalizing Flows*, *Mach. Learn. Sci. Tech.* **1** (2020) 4, 045023, [arXiv:2001.05486 \[physics.comp-ph\]](#).
- [19] E. Bothmann, T. Janßen, M. Knobbe, T. Schmale, and S. Schumann, *Exploring phase space with Neural Importance Sampling*, *SciPost Phys.* **8** (2020) 4, 069, [arXiv:2001.05478 \[hep-ph\]](#).
- [20] C. Gao, S. Höche, J. Isaacson, C. Krause, and H. Schulz, *Event Generation with Normalizing Flows*, *Phys. Rev. D* **101** (2020) 7, 076002, [arXiv:2001.10028 \[hep-ph\]](#).
- [21] K. Danziger, T. Janßen, S. Schumann, and F. Siegert, *Accelerating Monte Carlo event generation – rejection sampling using neural network event-weight estimates*, *SciPost Phys.* **12** (2022) 164, [arXiv:2109.11964 \[hep-ph\]](#).
- [22] T. Janßen, D. Maître, S. Schumann, F. Siegert, and H. Truong, *Unweighting multijet event generation using factorisation-aware neural networks*, *SciPost Phys.* **15** (2023) 107, [arXiv:2301.13562 \[hep-ph\]](#).
- [23] E. Bothmann, T. Childers, W. Giele, F. Herren, S. Hoeche, J. Isaacsson, M. Knobbe, and R. Wang, *Efficient phase-space generation for hadron collider event simulation*, *SciPost Phys.* **15** (2023) 169, [arXiv:2302.10449 \[hep-ph\]](#).
- [24] N. Deutschmann and N. Götz, *Accelerating HEP simulations with Neural Importance Sampling*, *JHEP* **03** (2024) 083, [arXiv:2401.09069 \[hep-ph\]](#).
- [25] S. Otten, S. Caron, W. de Swart, M. van Beekveld, L. Hendriks, C. van Leeuwen, D. Podareanu, R. Ruiz de Austri, and R. Verheyen, *Event Generation and Statistical Sampling for Physics with Deep Generative Models and a Density Information Buffer*, *Nature Commun.* **12** (2021) 1, 2985, [arXiv:1901.00875 \[hep-ph\]](#).
- [26] B. Hashemi, N. Amin, K. Datta, D. Olivito, and M. Pierini, *LHC analysis-specific datasets with Generative Adversarial Networks*, [arXiv:1901.05282 \[hep-ex\]](#).
- [27] R. Di Sipio, M. Fucci Giannelli, S. Ketabchi Haghighat, and S. Palazzo, *DijetGAN: A Generative-Adversarial Network Approach for the Simulation of QCD Dijet Events at the LHC*, *JHEP* **08** (2019) 110, [arXiv:1903.02433 \[hep-ex\]](#).
- [28] A. Butter, T. Plehn, and R. Winterhalder, *How to GAN LHC Events*, *SciPost Phys.* **7** (2019) 6, 075, [arXiv:1907.03764 \[hep-ph\]](#).
- [29] Y. Alanazi, N. Sato, T. Liu, W. Melnitchouk, M. P. Kuchera, E. Pritchard, M. Robertson, R. Strauss, L. Velasco, and Y. Li, *Simulation of electron-proton scattering events by a Feature-Augmented and Transformed Generative Adversarial Network (FAT-GAN)*, [arXiv:2001.11103 \[hep-ph\]](#).
- [30] A. Butter, T. Heimel, S. Hummerich, T. Krebs, T. Plehn, A. Rousselot, and S. Vent, *Generative networks for precision enthusiasts*, *SciPost Phys.* **14** (2023) 4, 078, [arXiv:2110.13632 \[hep-ph\]](#).
- [31] A. Butter, N. Huetsch, S. Palacios Schweitzer, T. Plehn, P. Sorrenson, and J. Spinner, *Jet Diffusion versus JetGPT – Modern Networks for the LHC*, [arXiv:2305.10475 \[hep-ph\]](#).

- [32] L. de Oliveira, M. Paganini, and B. Nachman, *Learning Particle Physics by Example: Location-Aware Generative Adversarial Networks for Physics Synthesis*, *Comput. Softw. Big Sci.* **1** (2017) 1, 4, [arXiv:1701.05927 \[stat.ML\]](#).
- [33] A. Andreassen, I. Feige, C. Frye, and M. D. Schwartz, *JUNIPR: a Framework for Unsupervised Machine Learning in Particle Physics*, *Eur. Phys. J. C* **79** (2019) 2, 102, [arXiv:1804.09720 \[hep-ph\]](#).
- [34] E. Bothmann and L. Debbio, *Reweighting a parton shower using a neural network: the final-state case*, *JHEP* **01** (2019) 033, [arXiv:1808.07802 \[hep-ph\]](#).
- [35] K. Dohi, *Variational Autoencoders for Jet Simulation*, [arXiv:2009.04842 \[hep-ph\]](#).
- [36] E. Buhmann, G. Kasieczka, and J. Thaler, *EPiC-GAN: Equivariant point cloud generation for particle jets*, *SciPost Phys.* **15** (2023) 4, 130, [arXiv:2301.08128 \[hep-ph\]](#).
- [37] M. Leigh, D. Sengupta, G. Quétant, J. A. Raine, K. Zoch, and T. Golling, *PC-JeDi: Diffusion for particle cloud generation in high energy physics*, *SciPost Phys.* **16** (2024) 1, 018, [arXiv:2303.05376 \[hep-ph\]](#).
- [38] V. Mikuni, B. Nachman, and M. Pettee, *Fast point cloud generation with diffusion models in high energy physics*, *Phys. Rev. D* **108** (2023) 3, 036025, [arXiv:2304.01266 \[hep-ph\]](#).
- [39] E. Buhmann, C. Ewen, D. A. Faroughy, T. Golling, G. Kasieczka, M. Leigh, G. Quétant, J. A. Raine, D. Sengupta, and D. Shih, *EPiC-ly Fast Particle Cloud Generation with Flow-Matching and Diffusion*, [arXiv:2310.00049 \[hep-ph\]](#).
- [40] M. Paganini, L. de Oliveira, and B. Nachman, *Accelerating Science with Generative Adversarial Networks: An Application to 3D Particle Showers in Multilayer Calorimeters*, *Phys. Rev. Lett.* **120** (2018) 4, 042003, [arXiv:1705.02355 \[hep-ex\]](#).
- [41] L. de Oliveira, M. Paganini, and B. Nachman, *Controlling Physical Attributes in GAN-Accelerated Simulation of Electromagnetic Calorimeters*, *J. Phys. Conf. Ser.* **1085** (2018) 4, 042017, [arXiv:1711.08813 \[hep-ex\]](#).
- [42] M. Paganini, L. de Oliveira, and B. Nachman, *CaloGAN : Simulating 3D high energy particle showers in multilayer electromagnetic calorimeters with generative adversarial networks*, *Phys. Rev. D* **97** (2018) 1, 014021, [arXiv:1712.10321 \[hep-ex\]](#).
- [43] M. Erdmann, L. Geiger, J. Glombitza, and D. Schmidt, *Generating and refining particle detector simulations using the Wasserstein distance in adversarial networks*, *Comput. Softw. Big Sci.* **2** (2018) 1, 4, [arXiv:1802.03325 \[astro-ph.IM\]](#).
- [44] M. Erdmann, J. Glombitza, and T. Quast, *Precise simulation of electromagnetic calorimeter showers using a Wasserstein Generative Adversarial Network*, *Comput. Softw. Big Sci.* **3** (2019) 1, 4, [arXiv:1807.01954 \[physics.ins-det\]](#).
- [45] D. Belayneh *et al.*, *Calorimetry with deep learning: particle simulation and reconstruction for collider physics*, *Eur. Phys. J. C* **80** (2020) 7, 688, [arXiv:1912.06794 \[physics.ins-det\]](#).
- [46] E. Buhmann, S. Diefenbacher, E. Eren, F. Gaede, G. Kasieczka, A. Korol, and K. Krüger, *Getting High: High Fidelity Simulation of High Granularity Calorimeters with High Speed*, *Comput. Softw. Big Sci.* **5** (2021) 1, 13, [arXiv:2005.05334 \[physics.ins-det\]](#).

- [47] E. Buhmann, S. Diefenbacher, E. Eren, F. Gaede, G. Kasieczka, A. Korol, and K. Krüger, *Decoding Photons: Physics in the Latent Space of a BIB-AE Generative Network*, *EPJ Web Conf.* **251** (2021) 03003, [arXiv:2102.12491 \[physics.ins-det\]](#).
- [48] C. Krause and D. Shih, *Fast and accurate simulations of calorimeter showers with normalizing flows*, *Phys. Rev. D* **107** (2023) 11, 113003, [arXiv:2106.05285 \[physics.ins-det\]](#).
- [49] ATLAS Collaboration, *AtlFast3: the next generation of fast simulation in ATLAS*, *Comput. Softw. Big Sci.* **6** (2022) 7, [arXiv:2109.02551 \[hep-ex\]](#).
- [50] C. Krause and D. Shih, *Accelerating accurate simulations of calorimeter showers with normalizing flows and probability density distillation*, *Phys. Rev. D* **107** (2023) 11, 113004, [arXiv:2110.11377 \[physics.ins-det\]](#).
- [51] E. Buhmann, S. Diefenbacher, D. Hundhausen, G. Kasieczka, W. Korcari, E. Eren, F. Gaede, K. Krüger, P. McKeown, and L. Rustige, *Hadrons, better, faster, stronger*, *Mach. Learn. Sci. Tech.* **3** (2022) 2, 025014, [arXiv:2112.09709 \[physics.ins-det\]](#).
- [52] C. Chen, O. Cerri, T. Q. Nguyen, J. R. Vlimant, and M. Pierini, *Analysis-Specific Fast Simulation at the LHC with Deep Learning*, *Comput. Softw. Big Sci.* **5** (2021) 1, 15.
- [53] V. Mikuni and B. Nachman, *Score-based generative models for calorimeter shower simulation*, *Phys. Rev. D* **106** (2022) 9, 092009, [arXiv:2206.11898 \[hep-ph\]](#).
- [54] ATLAS Collaboration, *Deep Generative Models for Fast Photon Shower Simulation in ATLAS*, *Comput. Softw. Big Sci.* **8** (2024) 1, 7, [arXiv:2210.06204 \[hep-ex\]](#).
- [55] C. Krause, I. Pang, and D. Shih, *CaloFlow for CaloChallenge Dataset 1*, *SciPost Phys.* **16** (2024) 126, [arXiv:2210.14245 \[physics.ins-det\]](#).
- [56] J. C. Cresswell, B. L. Ross, G. Loaiza-Ganem, H. Reyes-Gonzalez, M. Letizia, and A. L. Caterini, *CaloMan: Fast generation of calorimeter showers with density estimation on learned manifolds*, in *36th Conference on Neural Information Processing Systems*. 11, 2022. [arXiv:2211.15380 \[hep-ph\]](#).
- [57] S. Diefenbacher, E. Eren, F. Gaede, G. Kasieczka, C. Krause, I. Shekhzadeh, and D. Shih, *L2LFlows: generating high-fidelity 3D calorimeter images*, *JINST* **18** (2023) 10, P10017, [arXiv:2302.11594 \[physics.ins-det\]](#).
- [58] B. Hashemi, N. Hartmann, S. Sharifzadeh, J. Kahn, and T. Kuhr, *Ultra-high-granularity detector simulation with intra-event aware generative adversarial network and self-supervised relational reasoning*, *Nature Commun.* **15** (2024) 1, 5825, [arXiv:2303.08046 \[physics.ins-det\]](#).
- [59] A. Xu, S. Han, X. Ju, and H. Wang, *Generative machine learning for detector response modeling with a conditional normalizing flow*, *JINST* **19** (2024) 02, P02003, [arXiv:2303.10148 \[hep-ex\]](#).
- [60] S. Diefenbacher, E. Eren, F. Gaede, G. Kasieczka, A. Korol, K. Krüger, P. McKeown, and L. Rustige, *New angles on fast calorimeter shower simulation*, *Mach. Learn. Sci. Tech.* **4** (2023) 3, 035044, [arXiv:2303.18150 \[physics.ins-det\]](#).
- [61] E. Buhmann, S. Diefenbacher, E. Eren, F. Gaede, G. Kasieczka, A. Korol, W. Korcari, K. Krüger, and P. McKeown, *CaloClouds: fast geometry-independent highly-granular calorimeter simulation*, *JINST* **18** (2023) 11, P11025, [arXiv:2305.04847 \[physics.ins-det\]](#).

- [62] M. R. Buckley, C. Krause, I. Pang, and D. Shih, *Inductive simulation of calorimeter showers with normalizing flows*, *Phys. Rev. D* **109** (2024) 3, 033006, [arXiv:2305.11934 \[physics.ins-det\]](#).
- [63] S. Diefenbacher, V. Mikuni, and B. Nachman, *Refining Fast Calorimeter Simulations with a Schrödinger Bridge*, [arXiv:2308.12339 \[physics.ins-det\]](#).
- [64] F. Ernst, L. Favaro, C. Krause, T. Plehn, and D. Shih, *Normalizing Flows for High-Dimensional Detector Simulations*, [arXiv:2312.09290 \[hep-ph\]](#).
- [65] L. Favaro, A. Ore, S. P. Schweitzer, and T. Plehn, *CaloDREAM – Detector Response Emulation via Attentive flow Matching*, [arXiv:2405.09629 \[hep-ph\]](#).
- [66] T. Buss, F. Gaede, G. Kasieczka, C. Krause, and D. Shih, *Convolutional L2LFlows: Generating Accurate Showers in Highly Granular Calorimeters Using Convolutional Normalizing Flows*, [arXiv:2405.20407 \[physics.ins-det\]](#).
- [67] G. Quétant, J. A. Raine, M. Leigh, D. Sengupta, and T. Golling, *PIPPIN: Generating variable length full events from partons*, [arXiv:2406.13074 \[hep-ph\]](#).
- [68] A. Butter, S. Diefenbacher, G. Kasieczka, B. Nachman, and T. Plehn, *GANplifying event samples*, *SciPost Phys.* **10** (2021) 6, 139, [arXiv:2008.06545 \[hep-ph\]](#).
- [69] S. Bieringer, A. Butter, S. Diefenbacher, E. Eren, F. Gaede, D. Hundhausen, G. Kasieczka, B. Nachman, T. Plehn, and M. Trabs, *Calomplification — the power of generative calorimeter models*, *JINST* **17** (2022) 09, P09028, [arXiv:2202.07352 \[hep-ph\]](#).
- [70] R. Winterhalder, M. Bellagente, and B. Nachman, *Latent Space Refinement for Deep Generative Models*, [arXiv:2106.00792 \[stat.ML\]](#).
- [71] B. Nachman and R. Winterhalder, *Elsa: enhanced latent spaces for improved collider simulations*, *Eur. Phys. J. C* **83** (2023) 9, 843, [arXiv:2305.07696 \[hep-ph\]](#).
- [72] M. Leigh, D. Sengupta, J. A. Raine, G. Quétant, and T. Golling, *Faster diffusion model with improved quality for particle cloud generation*, *Phys. Rev. D* **109** (2024) 1, 012010, [arXiv:2307.06836 \[hep-ex\]](#).
- [73] R. Das, L. Favaro, T. Heimel, C. Krause, T. Plehn, and D. Shih, *How to understand limitations of generative networks*, *SciPost Phys.* **16** (2024) 1, 031, [arXiv:2305.16774 \[hep-ph\]](#).
- [74] A. Butter, T. Plehn, and R. Winterhalder, *How to GAN Event Subtraction*, *SciPost Phys. Core* **3** (2020) 009, [arXiv:1912.08824 \[hep-ph\]](#).
- [75] B. Stienen and R. Verheyen, *Phase space sampling and inference from weighted events with autoregressive flows*, *SciPost Phys.* **10** (2021) 2, 038, [arXiv:2011.13445 \[hep-ph\]](#).
- [76] M. Backes, A. Butter, T. Plehn, and R. Winterhalder, *How to GAN Event Unweighting*, *SciPost Phys.* **10** (2021) 4, 089, [arXiv:2012.07873 \[hep-ph\]](#).
- [77] F. A. Di Bello, S. Ganguly, E. Gross, M. Kado, M. Pitt, L. Santi, and J. Shlomi, *Towards a Computer Vision Particle Flow*, *Eur. Phys. J. C* **81** (2021) 2, 107, [arXiv:2003.08863 \[physics.data-an\]](#).

- [78] P. Baldi, L. Blecher, A. Butter, J. Collado, J. N. Howard, F. Keilbach, T. Plehn, G. Kasieczka, and D. Whiteson, *How to GAN Higher Jet Resolution*, *SciPost Phys.* **13** (2022) 3, 064, [arXiv:2012.11944 \[hep-ph\]](#).
- [79] K. Datta, D. Kar, and D. Roy, *Unfolding with Generative Adversarial Networks*, [arXiv:1806.00433 \[physics.data-an\]](#).
- [80] M. Bellagente, A. Butter, G. Kasieczka, T. Plehn, and R. Winterhalder, *How to GAN away Detector Effects*, *SciPost Phys.* **8** (2020) 4, 070, [arXiv:1912.00477 \[hep-ph\]](#).
- [81] A. Andreassen, P. T. Komiske, E. M. Metodiev, B. Nachman, and J. Thaler, *OmniFold: A Method to Simultaneously Unfold All Observables*, *Phys. Rev. Lett.* **124** (2020) 18, 182001, [arXiv:1911.09107 \[hep-ph\]](#).
- [82] M. Bellagente, A. Butter, G. Kasieczka, T. Plehn, A. Rousselot, R. Winterhalder, L. Ardizzone, and U. Köthe, *Invertible Networks or Partons to Detector and Back Again*, *SciPost Phys.* **9** (2020) 074, [arXiv:2006.06685 \[hep-ph\]](#).
- [83] M. Backes, A. Butter, M. Dunford, and B. Malaescu, *An unfolding method based on conditional Invertible Neural Networks (cINN) using iterative training*, [arXiv:2212.08674 \[hep-ph\]](#).
- [84] M. Leigh, J. A. Raine, K. Zoch, and T. Golling, *ν -flows: Conditional neutrino regression*, *SciPost Phys.* **14** (2023) 6, 159, [arXiv:2207.00664 \[hep-ph\]](#).
- [85] J. A. Raine, M. Leigh, K. Zoch, and T. Golling, *Fast and improved neutrino reconstruction in multineutrino final states with conditional normalizing flows*, *Phys. Rev. D* **109** (2024) 1, 012005, [arXiv:2307.02405 \[hep-ph\]](#).
- [86] A. Shmakov, K. Greif, M. Fenton, A. Ghosh, P. Baldi, and D. Whiteson, *End-To-End Latent Variational Diffusion Models for Inverse Problems in High Energy Physics*, [arXiv:2305.10399 \[hep-ex\]](#).
- [87] J. Ackerschott, R. K. Barman, D. Gonçalves, T. Heimel, and T. Plehn, *Returning CP-Observables to The Frames They Belong*, *SciPost Phys.* **17** (2024) 001, [arXiv:2308.00027 \[hep-ph\]](#).
- [88] S. Diefenbacher, G.-H. Liu, V. Mikuni, B. Nachman, and W. Nie, *Improving Generative Model-based Unfolding with Schrödinger Bridges*, [arXiv:2308.12351 \[hep-ph\]](#).
- [89] S. Bieringer, A. Butter, T. Heimel, S. Höche, U. Köthe, T. Plehn, and S. T. Radev, *Measuring QCD Splittings with Invertible Networks*, *SciPost Phys.* **10** (2021) 6, 126, [arXiv:2012.09873 \[hep-ph\]](#).
- [90] A. Butter, T. Heimel, T. Martini, S. Peitzsch, and T. Plehn, *Two invertible networks for the matrix element method*, *SciPost Phys.* **15** (2023) 3, 094, [arXiv:2210.00019 \[hep-ph\]](#).
- [91] T. Heimel, N. Huetsch, R. Winterhalder, T. Plehn, and A. Butter, *Precision-Machine Learning for the Matrix Element Method*, [arXiv:2310.07752 \[hep-ph\]](#).
- [92] H. Du, C. Krause, V. Mikuni, B. Nachman, I. Pang, and D. Shih, *Unifying Simulation and Inference with Normalizing Flows*, [arXiv:2404.18992 \[hep-ph\]](#).
- [93] B. Nachman and D. Shih, *Anomaly Detection with Density Estimation*, *Phys. Rev. D* **101** (2020) 075042, [arXiv:2001.04990 \[hep-ph\]](#).

- [94] A. Hallin, J. Isaacson, G. Kasieczka, C. Krause, B. Nachman, T. Quadfasel, M. Schlaffer, D. Shih, and M. Sommerhalder, *Classifying anomalies through outer density estimation*, *Phys. Rev. D* **106** (9, 2022) 055006, [arXiv:2109.00546 \[hep-ph\]](#).
- [95] J. A. Raine, S. Klein, D. Sengupta, and T. Golling, *CURTAINS for your sliding window: Constructing unobserved regions by transforming adjacent intervals*, *Front. Big Data* **6** (2023) 899345, [arXiv:2203.09470 \[hep-ph\]](#).
- [96] A. Hallin, G. Kasieczka, T. Quadfasel, D. Shih, and M. Sommerhalder, *Resonant anomaly detection without background sculpting*, *Phys. Rev. D* **107** (2023) 11, 114012, [arXiv:2210.14924 \[hep-ph\]](#).
- [97] T. Golling, S. Klein, R. Mastandrea, and B. Nachman, *Flow-enhanced transportation for anomaly detection*, *Phys. Rev. D* **107** (2023) 9, 096025, [arXiv:2212.11285 \[hep-ph\]](#).
- [98] D. Sengupta, S. Klein, J. A. Raine, and T. Golling, *CURTAINS Flows For Flows: Constructing Unobserved Regions with Maximum Likelihood Estimation*, [arXiv:2305.04646 \[hep-ph\]](#).
- [99] L. Heinrich and M. Kagan, *Differentiable Matrix Elements with MadJax*, *J. Phys. Conf. Ser.* **2438** (2023) 1, 012137, [arXiv:2203.00057 \[hep-ph\]](#).
- [100] MODE, T. Dorigo *et al.*, *Toward the end-to-end optimization of particle physics instruments with differentiable programming*, *Rev. Phys.* **10** (2023) 100085, [arXiv:2203.13818 \[physics.ins-det\]](#).
- [101] M. Kagan and L. Heinrich, *Branches of a Tree: Taking Derivatives of Programs with Discrete and Branching Randomness in High Energy Physics*, [arXiv:2308.16680 \[stat.ML\]](#).
- [102] M. Aehle, M. Novák, V. Vassilev, N. R. Gauger, L. Heinrich, M. Kagan, and D. Lange, *Optimization Using Pathwise Algorithmic Derivatives of Electromagnetic Shower Simulations*, [arXiv:2405.07944 \[physics.comp-ph\]](#).
- [103] B. Nachman and S. Prestel, *Morphing parton showers with event derivatives*, [arXiv:2208.02274 \[hep-ph\]](#).
- [104] F. Maltoni and T. Stelzer, *MadEvent: Automatic event generation with MadGraph*, *JHEP* **02** (2003) 027, [arXiv:hep-ph/0208156](#).
- [105] O. Mattelaer and K. Ostrolenk, *Speeding up MadGraph5_aMC@NLO*, *Eur. Phys. J. C* **81** (2021) 5, 435, [arXiv:2102.00773 \[hep-ph\]](#).
- [106] R. Kleiss and R. Pittau, *Weight optimization in multichannel Monte Carlo*, *Comput. Phys. Commun.* **83** (1994) 141, [arXiv:hep-ph/9405257](#).
- [107] S. Weinzierl, *Introduction to Monte Carlo methods*, [arXiv:hep-ph/0006269](#).
- [108] W. Kilian, T. Ohl, and J. Reuter, *WHIZARD: Simulating Multi-Particle Processes at LHC and ILC*, *Eur. Phys. J. C* **71** (2011) 1742, [arXiv:0708.4233 \[hep-ph\]](#).
- [109] L. Ardizzone, J. Kruse, S. Wirkert, D. Rahner, E. W. Pellegrini, R. S. Klessen, L. Maier-Hein, C. Rother, and U. Köthe, *Analyzing inverse problems with invertible neural networks*, International Conference on Learning Representations (2018) , [arXiv:1808.04730 \[cs.LG\]](#).

- [110] I. Kobyzev, S. Prince, and M. Brubaker, *Normalizing flows: An introduction and review of current methods*, *IEEE Transactions on Pattern Analysis and Machine Intelligence* (2020) 1–1, [arXiv:1908.09257 \[stat.ML\]](#).
- [111] G. P. Lepage, *A New Algorithm for Adaptive Multidimensional Integration*, *J. Comput. Phys.* **27** (1978) 192.
- [112] G. P. Lepage, *VEGAS: AN ADAPTIVE MULTIDIMENSIONAL INTEGRATION PROGRAM*, .
- [113] G. P. Lepage, *Adaptive multidimensional integration: VEGAS enhanced*, *J. Comput. Phys.* **439** (2021) 110386, [arXiv:2009.05112 \[physics.comp-ph\]](#).
- [114] A. Butter, S. Diefenbacher, G. Kasieczka, B. Nachman, T. Plehn, D. Shih, and R. Winterhalder, *Ephemeral Learning - Augmenting Triggers with Online-Trained Normalizing Flows*, *SciPost Phys.* **13** (2022) 4, 087, [arXiv:2202.09375 \[hep-ph\]](#).
- [115] W. H. Press and G. R. Farrar, *Recursive stratified sampling for multidimensional monte carlo integration*, *Computers in Physics* **4** (1990) 2, 190.
- [116] S. Carrazza, J. Cruz-Martinez, M. Rossi, and M. Zaro, *MadFlow: automating Monte Carlo simulation on GPU for particle physics processes*, *Eur. Phys. J. C* **81** (2021) 7, 656, [arXiv:2106.10279 \[physics.comp-ph\]](#).
- [117] R. Kleiss, W. Stirling, and S. Ellis, *A new monte carlo treatment of multiparticle phase space at high energies*, *Computer Physics Communications* **40** (1986) 2, 359.
- [118] S. Plätzer, *RAMBO on diet*, [arXiv:1308.2922 \[hep-ph\]](#).
- [119] M. R. Whalley, D. Bourilkov, and R. C. Group, *The Les Houches accord PDFs (LHAPDF) and LHAGLUE*, in *HERA and the LHC: A Workshop on the Implications of HERA and LHC Physics (Startup Meeting, CERN, 26-27 March 2004; Midterm Meeting, CERN, 11-13 October 2004)*. 8, 2005. [arXiv:hep-ph/0508110](#).
- [120] S. Carrazza, J. M. Cruz-Martinez, and M. Rossi, *PDFFlow: Parton distribution functions on GPU*, *Comput. Phys. Commun.* **264** (2021) 107995, [arXiv:2009.06635 \[hep-ph\]](#).
- [121] F. Nielsen and R. Nock, *On the chi square and higher-order chi distances for approximating f -divergences*, *IEEE Signal Processing Letters* **21** (Jan, 2014) 10–13, [arXiv:1309.3029 \[cs.IT\]](#).
- [122] S. Dittmaier and M. Roth, *LUSIFER: A LUCid approach to six FERMion production*, *Nucl. Phys. B* **642** (2002) 307, [arXiv:hep-ph/0206070](#).
- [123] D. P. Kingma and J. Ba, *Adam: A Method for Stochastic Optimization*, [arXiv:1412.6980 \[cs.LG\]](#).
- [124] C. Durkan, A. Bekasov, I. Murray, and G. Papamakarios, *Neural spline flows*, *Advances in Neural Information Processing Systems* **32** (6, 2019) 7511, [arXiv:1906.04032 \[stat.ML\]](#).